Numerical prediction of cavitation for a horizontal axis tidal turbine

Adriano Evangelisti[1, 2*], Giuliano Agati[3], Domenico Borello[3], Luca Mazzotta[1, 4], Paolo Capobianchi[2] and Paolo Venturini[3]

[1] Department of Astronautical, Electrical and Energy Engineering, Sapienza University of Rome, Via Eudossiana 18, Rome, 00184, Italy.

[2] James Weir Fluids Laboratory, Department of Mechanical and Aerospace Engineering, University of Strathclyde, Glasgow, G1 1XJ, United Kingdom.

[3] Department of Mechanical and Aerospace Engineering, Sapienza University of Rome, Via Eudossiana 18, Rome, 00184, Italy.

[4] Baker Hughes, Via Felice Matteucci 2, Florence, 50127, Italy.

*Corresponding author. E-mail: adriano.evangelisti@uniroma1.it;

Contributing authors. E-mails: giuliano.agati@uniroma1.it; domenico.borello@uniroma1.it; luca.mazzotta@uniroma1.it; paolo.capobianchi@strath.ac.uk; paolo.venturini@uniroma1.it.

Abstract

This paper aims at assessing cavitation in a scaled tidal turbine geometry through numerical simulations. Cavitation occurrence is predicted by using the Singhal cavitation model, based on the Rayleigh-Plesset equation, for treating bubble dynamics. Turbulence is modelled adopting a Reynolds Averaged Navier Stokes (RANS) approach, specifically employing the Shear Stress Transport (SST) $k-\omega$ model to simulate the fluid flow. The Reboud density function is applied to adjust the eddy viscosity computation in the cavitation region. Initially, cavitation and turbulence models are validated using a NACA 66 (mod) hydrofoil profile as a test case. Numerical and experimental pressure coefficients are compared on the hydrofoil suction side for a selected cavitation condition. A Mesh Sensitivity Analysis (MSA) is performed to ensure simulation accuracy, comparing numerical results with experimental data on the Horizontal Axis Tidal Turbine (HATT) scaled domain. Based on this analysis, the optimal computational grid is selected. Experimental and numerical power and thrust coefficients are then compared across different tip speed ratios. Finally, cavitation occurrence is evaluated for four different regimes, namely the cut-in, the peak-power, the curve highest velocity and the off-set tip speed ratios. Computational Fluid Dynamics (CFD) solutions

reveal vapor formation around turbine components, highlighting regions most exposed to cavitation onset.

Keywords: CFD; cavitation; bubble dynamics; MSA; HATT

Latin symbols

a	Water density-correction exponent, (-)
c	Chord length, (m)
C	Numerical coefficient, (m/s) (-) / model constants
f	Gaseous mass fraction, (-)
f	Density function, (kg/m^3)
F	Total thrust force, (N)
k	Turbulent kinetic energy, (J/kg)
m	Mass, (kg)
$\dot{m}$	Net cavitation mass rate – per unit volume, (kg/(m^{3}s))
$\dot{M}$	Mass flow rate, (kg/s)
n	Number density, (1/m^3)
p	Static pressure, (Pa)
q	One-blade torque, (N m)
Q	Total power (W)
R	Radius, (m)
R	Reynolds stress tensor, (kg/m s^2)
Re	Reynolds number, (-)
t	Time, (s)
T	Total thrust, (N)
U	Flow velocity, (m/s)
v	Total velocity, (m/s)
V	Volume, (m^3)
w	Angular velocity, (rad/s)
x, y, z	Cartesian coordinates, (m)
y^+	Wall y-plus, (-)

Greek symbols

α	Vapour volume fraction, (-)
β	Angle of attack, (°)
γ	Liquid-vapour water surface tension, (N/m)
ε	Relative error, (%)
λ	Tip speed ratio, (-)
μ	Water mixture dynamic viscosity, (Pa s)
ν	Kinematic viscosity, (m^2/s)

ρ	Water mixture density, (kg/m^3)
σ	Cavitation number, (-)
τ	One-blade thrust force, (N)
ω	Specific dissipation rate, (1/s)
Subscripts	
B	Bubble(s)
c	Condensation process
e	Evaporation process
F	Thrust-related variables
g	Non condensable gaseous species
H	Hydrofoil parameters
i (j)	Cartesian coordinates components
l	Liquid water
out	Outlet-reference conditions
p	Pressure-related variables
Q	Power-related variables
R	Reboud correction
S	Standard RANS computation
T	Turbine parameters
v	Vapour water
τ	Turbulent variables
∞	Far field conditions
1-7	SST k-ω constants
Superscripts	
CFD	*CFD* numerical values
EXP	*EXP* data
EXP - CFD	Difference between *EXP* data and *CFD* numerical values
Abbreviations	
CFD	Computational Fluid Dynamics
EXP	Experimental Data
HATT	Horizontal Axis Tidal Turbine
MRF	Multiple Reference Frame
MSA	Mesh Sensitivity Analysis
NCG	Non-Condensable Gas
RANS	Raynolds Averaged Navier Stokes
SST	Shear Stress Transport
TSR	Tip Speed Ratio
UDF	User Define Function

1 Introduction

When a sharp drop in the liquid head causes the static pressure to fall below the saturated vapour pressure, a physical transition from liquid to vapour is triggered. This phenomenon is known in the literature as cavitation (Young, 1999). It is characterized by the nucleation of gas-filled bubbles which can grow until the external pressure remains below the vapour tension. Huge hydrostatic head reductions are often encountered in fluid machines such as pumps, hydraulic turbines, injectors, hydrofoil wings, etc. When the surrounding flow brings the vapour entities into higher head zones, i.e., when the static pressure is again higher than the vapour tension, a sudden implosion of the vapour volumes occurs (Gohil & Saini, 2014). The implosion mechanism leads to the formation of liquid jets in the final stage of the bubble life. If an implosion event is localized close to a solid wall, the formed jet can hit the exposed surface. The repetition of these impacts over time can cause erosion of the target material (Dular et al., 2006). For these reasons, the possibility of cavitation initiation in the flow field around the hydraulic machine components must be verified during the design process. In this context, coating materials and inducers are some of the solutions studied to mitigate the cavitation erosion damage (Hong et al., 2021).

The modelling of cavitation involves many fluid dynamics features that need to be evaluated. In the past years, several approaches were tested to model analytically the cavitation phenomenon. In fact, different engineering applications are based on the implementation of the so-called homogeneous mixture models, suitable to reproduce large-scale cavitation phenomena (Ghahramani et al., 2021). These models are also divided into barotropic and transport equation models (Savio et al., 2021). The first group is generally used to assess the effect of chocking on the liquid flow rate, although poor prediction of cavitation dynamics is recognized under turbulent flow conditions (Ducoin et al., 2012). On the other hand, the transport equation modelling approaches are widely used, thanks to the introduction of the net mass transfer rate equation, related to the definition of the source and sink terms: the evaporation and condensation rates, respectively. Merkle et al. (1998) and Kunz et al. (2000), developed models which link the source and sink terms of the transport equation to the mixture density variations. The Saito et al. (2007) cavitation model is particularly suited to investigate cavitation for planar geometry. For interphase problems, the implementation of the model of Senocak and Shyy (2002) is commonly suggested while the most renowned cavitation models, belonging to the transport equation group, are the Singhal et al. (2003), Zwart et al. (2004) and Schnerr and Sauer (2001) models. They all use the Rayleigh-Plesset bubble dynamics equation (Young, 1999), for non-compressible flows, to evaluate the source and sink terms. The introduction of the bubble number density represents a key parameter for estimating the net mass transfer rate. When cavitation needs to be investigated for complex geometries, bubble dynamics models find wide application, as in the case of cavitation inception around pumps, ship propellers, hydraulic turbines, etc. As stated by Lee et al. (2021), the comparison of the model of Schnerr and Sauer (2001) with that of Merkle et al. (1998), highlighted a better performance in approaching the experimental data available for a NACA 66 hydrofoil propeller, when subjected to cavitation. Morgut et al. (2011), demonstrated a good interpretation of the Zwart et al. (2004) model when hybrid turbulence models such as Scale Adaptive Simulation (SAS) were used to replace the Reynolds Averaged Navier Stokes (RANS) approach, for both a Kaplan turbine and a marine-ship propeller. Cavitation inception and its temporal evolution are mainly influenced by geometry and flow conditions. These effects on the cavitating flows have been studied

in detail using calibration procedures of the coefficients of the rate equations, as reported in the works of Morgut et al. (2011) and Bilus et al. (2013). For non-compressible fluid flows, the bubble dynamics cavitation models based on the Reyleigh-Plesset equation, represent a reliable choice, providing stability in approaching convergence conditions, easiness to be implemented and accuracy in results prediction (Folden & Aschmoneit, 2023).

As cavitation occurrence is strictly related to the flow regions where pressure drops and velocity increases, different cavitation formations are recognized according to the rotor design. In this regard, Pelton turbines are particularly affected by cavitation inception in proximity of the needles and nozzles runner buckets while Kaplan and Francis turbines show the wider formations of vapour cavities on the runner and draft tube cones (Padhy & Saini, 2008). Tidal turbines, instead, due to a different shape of the rotor, exhibit different cavitation regimes. Shi et al. (2016), Capone et al. (2023) and Sun et al. (2022) reported how vapour mainly develops along the radial upper part of the blade extent in form of attached cavities located close to the leading-edge and blade suctions side, affected by tip vortexes formation where the highest rotating velocities are reached.

Tidal turbines are an evolving technology, with many engineering approaches focusing on establishing robust design procedures to ensure a long service life. As reported by Shi et al. (2016), cavitation poses a serious threat to the operating regimes of these hydraulic machines. Consequently, the occurrence of cavitation is a significant problem that must be addressed. Moreover, the effect of cavitation occurrence could be aggravated by sea fouling and solid particle erosion (Song et al., 2020). Among the different possibilities of counteracting the detrimental effects of cavitation, new composite materials are still being developed. When cavitation acts over time, its final erosive effect produces a damaged surface, covered with superficial diffuse cracks. Alam et al. (2018) explained how the external coatings can prevent the penetration of aggressive seawater agents into the target materials, acting as sacrificial layer in the erosion process. Cavitation formation strongly depends on the involved geometries as well as the fluid flow conditions, which in turn are affected by the blade-rotor design, and the material surface properties. Influence of angles of attack and flow conditions were experimentally analyzed in the works of Kravtsova et al. (2014) and Timoshevskiy et al. (2016) with the aim of assessing their incidence on the resulting cavitation regimes occurring on a NACA 0015 hydrofoil and a scaled-down model of guide vanes of a high-pressure turbine. The effects of surface roughness, instead, were experimentally investigated by Churkin et al. (2016) always on a NACA 0015 hydrofoil profile by means of high-speed visualizations, evaluating the effect on the dynamics of the attached sheet cavitation for different cavitating regimes at different angles of attack. On the other hand, Shi et al. (2016) investigated the possibility of designing hydraulic profiles equipped with leading-edge tubercules demonstrating a reduced extent of the cloud cavitation compared to standard turbine blades. Mitigation of cavitation severity was also investigated on a 2D hydrofoil by injecting a wall flux along the spanwise width of the profile (Timoshevskiy et al., 2018). Experimental results showed practical methods to manipulate and control cavitation-induced instabilities, which can further lead to vapour collapses and material damage.

In this scenario, the present paper aims to investigate the risk of cavitation for a scaled geometry tidal turbine for different operating conditions. The assessment of the cavitating flow fields comes at the end of a twofold validation process. On the one hand, the ability of the modelling approach to reproduce the turbulence-cavitation interaction is analyzed on a NACA 66 (mod) hydrofoil profile. On the other hand, a Mesh Sensitivity Analysis (MSA) is conducted on a Horizontal Axis Tidal Turbine (HATT) scaled domain to find the most appropriate computational grid and to validate the simulation results in terms of predicted power coefficients. The paper is organized

as follows: Section 2 presents the adopted models for both turbulence and cavitation phenomena, in Section 3 the main computational details are given for the validation test case (combination of turbulence and cavitation modelling) and the tidal turbine under analysis (identification of the optimal computational grid in terms of power and thrust coefficients prediction), Section 4 is finally dedicated to the discussion of the results, related to the prediction of cavitation formation for the tidal turbine.

2 Mathematical models

This Section presents numerical details concerning the selected mathematical models. The Reynolds Averaged Navier Stokes (RANS) equations are adopted to simulate the turbulent and cavitating flows. Equations' closure is realized by means of a two-equation turbulence model, properly corrected for the cavitating regime treatment (Sub-section 2.1). Cavitation is predicted adopting the Singhal et al. (2003) cavitation model and its formulation is explained in depth in Sub-section 2.2.

2.1 Turbulence modelling

The fluid dynamics equations are discretized adopting a RANS approach. In particular, turbulence is modelled using the two-equation SST k-ω model for both steady and unsteady simulations. This model is particularly suitable in treating the adverse pressure gradients and flow separation, as it occurs in the liquid flows around hydraulic machine components (Menter, 1993). Moreover, according to previous studies (Ellis et al., 2018 and Evangelisti et al., 2023a), the SST k-ω model was selected for numerical simulations of the considered tidal turbine, showing good alignment with the experimental data. The above-mentioned reasons lead the authors of the present work to select this model for CFD simulations, as well.

The structure of the SST formulation allows to switch to a k-ε treatment in the far field regions. This feature confers stability in approaching convergence, and reduces the sensitivity of the model to the inflow turbulence conditions. The model equations for transport of turbulent kinetic energy k (eq. (1)) and specific dissipation rate ω (eq. (2)) are reported below:

$$\frac{\partial(\rho k)}{\partial t}+U_j\frac{\partial(\rho k)}{\partial x_j}=\mathrm{R}_{ij}\frac{\partial U_i}{\partial x_j}-C_1\rho\omega k+\frac{\partial}{\partial x_j}\left[\left(\mu+C_2\mu_\tau\right)\frac{\partial k}{\partial x_j}\right] \tag{1}$$

$$\begin{aligned}\frac{\partial(\rho\omega)}{\partial t}+U_j\frac{\partial(\rho\omega)}{\partial x_j}&=\frac{\rho C_3}{\mu_\tau}\mathrm{R}_{ij}\frac{\partial U_i}{\partial x_j}-C_4\rho\omega^2 k+\\&+\frac{\partial}{\partial x_j}\left[\left(\mu+C_5\mu_\tau\right)\frac{\partial\omega}{\partial x_j}+2\left(1-C_6\right)\rho C_7\frac{1}{\omega}\frac{\partial k}{\partial x_j}\frac{\partial\omega}{\partial x_j}\right]\end{aligned} \tag{2}$$

where t is the flow time, x_j is the generic cartesian coordinate, ρ is the water mixture density, U_i and U_j are the velocity vector components, R_{ij} is the Reynolds stress tensor ($\mathrm{R}_{ij}=-\rho\overline{U_i'U_j'}$ with U_i' and U_j' being the velocity vector fluctuations), μ and μ_τ are the dynamic viscosity and the turbulent dynamic viscosity, respectively. Finally, $C_{1\text{-}7}$ are model's constants (Menter, 1993).

To assess the unsteadiness of the cavitation phenomenon, the computation of the turbulent viscosity is properly corrected by introducing the density function proposed by Reboud et al. (1998); the latter avoids numerical overestimations in the cavitating regions:

$$\mu_\tau \propto \frac{k}{\omega} f_R(\rho) \tag{3}$$

In eq. (3) f_r is the Reboud corrective function, defined as:

$$f_R(\rho) = \rho_v + \frac{(\rho - \rho_v)^a}{(\rho_l - \rho_v)^{a-1}} \tag{4}$$

where ρ_l and ρ_v represents the densities of the liquid and vapour phases, respectively. The a-exponent is chosen equal to 10 for water (Reboud et al., 1998). It is important to state that, in the ordinary RANS models the Reboud corrective function is replaced by the standard density function f_s:

$$f_S(\rho) = \rho \tag{5}$$

Noting the proportionality law between dynamic turbulent viscosity and density function, the effect of the aforementioned numerical correction can be observed by comparing the trends of eq. (4) and eq. (5) plotted in Fig. 1.

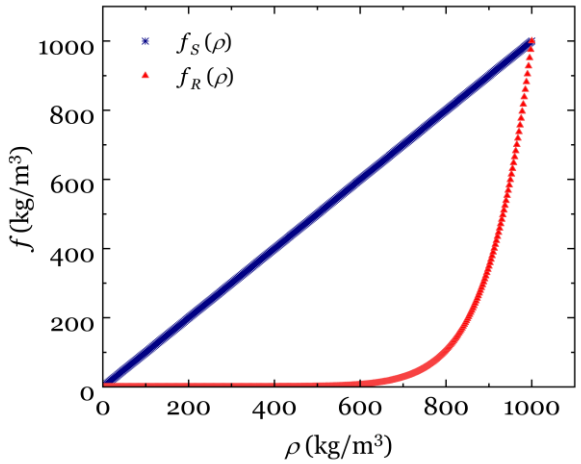

Fig. 1 Reboud and standard density functions, plotted from eqs. (4, 5), as function of the water mixture density ρ.

2.2 Cavitation modeling

The chosen cavitation model is based on the bubble dynamics equation, which was firstly elaborated in its non-compressible form by Rayleigh-Plesset (Young, 1999):

$$\frac{p_v(t) - p_\infty(t)}{\rho_l} = R_B \frac{d^2 R_B}{dt^2} + \frac{3}{2}\left(\frac{dR_B}{dt}\right)^2 + \frac{4\nu_l}{R_B}\frac{dR_B}{dt} + \frac{2\gamma}{\rho_l R_B} \tag{6}$$

where p_v and p_∞ are the vapour and the far field static pressures, R_B is the bubble radius, ν_l is the kinematic viscosity of the liquid water phase and γ is the liquid-vapour water surface tension.

The mathematical structure of eq. (6) is quite complex; therefore, a first order

approximation is often used to calculate the bubble radius velocity. The time dependent bubble-radius variation represents the link between the bubble dynamics treatment and the quantification of mass transfer:

$$\frac{dR_B}{dt} = \sqrt{\frac{2}{3}\frac{p_v(t) - p_\infty(t)}{\rho_l}} \tag{7}$$

Eq. (7) is analytically derived from eq. (6) by neglecting the second derivative, the viscous and the surface tension terms, as explained by Bernsten et al. (2001). As bubble dynamics cavitation models belong to the group of the homogeneous mixture cavitation models, fluids properties are expressed as a weighted average of the vapour volume fraction α, which is function of the involved phases' volumes: V_l for liquid water and V_v for vapour water, respectively:

$$\alpha = \frac{V_v}{V_l + V_v} \tag{8}$$

In this case ρ can be expressed as:

$$\rho(\alpha) = (1-\alpha)\rho_l + \alpha\rho_v \tag{9}$$

The main governing equations of the model are described by phases continuity. Using eq. (9), one can write the mass balance for both the liquid (eq. (10)) and vapour (eq. (11)) phases, where the source term $\dot{m}$ represents the net mass transfer rate due to cavitation:

$$-\frac{\dot{m}}{\rho_l} = \frac{\partial}{\partial t}(1-\alpha) + \frac{\partial}{\partial x_j}\left((1-\alpha)U_j\right) \tag{10}$$

$$\frac{\dot{m}}{\rho_v} = \frac{\partial}{\partial t}(\alpha) + \frac{\partial}{\partial x_j}\left(\alpha U_j\right) \tag{11}$$

Summation of corresponding terms in eqs. (10, 11) returns an expression for the velocity divergence operator, adapted to cavitating conditions:

$$\dot{m}\left(\frac{1}{\rho_v} - \frac{1}{\rho_l}\right) = \frac{\partial U_j}{\partial x_j} \tag{12}$$

Then, combination of vapour volume fraction material derivative ($d\alpha/dt$), derived from eq. (11) and velocity divergence expression, as reported in the right-hand side of eq. (12), allows to explicit a general form for $\dot{m}$:

$$\dot{m} = \frac{\rho_l \rho_v}{\rho}\frac{d\alpha}{dt} \tag{13}$$

The diversification that identifies the chosen cavitation model is obtained by introducing the characteristic definition of the bubble number density n_B according to Singhal et al. (2003):

$$\alpha = n_B V_B = {}^{4}\!/_{3}\,\pi n_B R_B^3 \tag{14}$$

In eq. (14) V_B represents the bubble volume. From eq. (14) $\alpha = \alpha(R_B)$, in this case the material derivative reported in the right-hand side of eq. (13) can be related to the term $(d/dt)R_B^3$. After some mathematics, re-expressing n_B as function of α and R_B, one can state:

$$\dot{m} = \frac{3\alpha}{R_B}\frac{\rho_l \rho_v}{\rho}\sqrt{\frac{2}{3}\frac{p_v - p_\infty}{\rho_l}} \tag{15}$$

Further improvements, added to this equation form, concern other fluid flow features, such as the influence of the turbulent kinetic energy on the phase transition process and the role of the surface tension on the development of the bubble radius. Moreover, it was empirically found that the single rate equation is proportional to the donor phase mass fractions, i.e., vapour is generated by liquid evaporation and liquid from vapour condensation f_v, conversely. The extended and detailed model form, as described by Singhal et al. (2003) also considers the presence of other non-condensable gases f_g (as the trapped air amount). The model rate equations were adapted to evaporation ($p_v \geq p_\infty$) and condensation ($p_v < p_\infty$), respectively:

if $p_v \geq p_\infty$:

$$\dot{m}_e = C_e \frac{\max\left(1.0; \sqrt{k}\right)}{\gamma}\rho_l \rho_v \sqrt{\frac{2}{3}\frac{p_v - p_\infty}{\rho_l}}\left(1 - f_v - \sum_g f_g\right) \tag{16.a}$$

if $p_v < p_\infty$:

$$\dot{m}_c = C_c \frac{\max\left(1.0; \sqrt{k}\right)}{\gamma}\rho_l^2 \sqrt{\frac{2}{3}\frac{p_\infty - p_v}{\rho_l}}\, f_v \tag{16.b}$$

Eqs. (16.a, 16.b) show the model equations in their final form, as implemented in the CFD solver (ANSYS Inc., 2021b). According to the work of the model authors (Singhal et al., 2003), the adopted values of the empirical coefficients are C_e = 0.02 m/s and C_c = 0.01 m/s.

3 Computational details

This Section provides a detailed discussion of numerical aspects related to the simulations' setup. The validation of cavitation and turbulence models, as well as the validation of the scaled geometry reproducing the tidal turbine, are described separately. In Sub-section 3.1, computational details are provided for the test case used to validate the combination of the corrected turbulence model and the Singhal et al. (2003) cavitation model. Sub-section 3.2 presents the specifics of the simulation conducted on the HATT and outlines the MSA procedure employed to select the optimal turbine mesh. Finally, validation results are presented in Sub-section 3.3. The validated models will be combined for the final cavitation study, as described in section 4. All simulations are performed using the commercial software Ansys Fluent, v21R2 (ANSYS Inc., 2021a, 2021b, 2021c).

3.1 Test case domain

A test case domain from the literature is selected for validating the combination of the Singhal et al. (2003) cavitation model and the SST k-ω turbulence model (Menter, 1993), with the introduction of the eddy viscosity correction (Reboud et al., 1998). Eq. (1) is implemented within the solver by means of a User Defined Function (UDF), (ANSYS Inc., 2021a). The NACA 66 (mod) profile, as used in the work of Shen and Dimotakis (1989), with a reference chord length c_H = 0.15 m, is adopted as test case. Domain maximum dimensions, scaled by the hydrofoil chord length, are 7 c_H × 3.5 c_H × 0.1 c_H, along the x, y and z coordinates, respectively. The computational domain and the adopted boundary conditions (BCs) are illustrated in Fig. 2.

The inlet velocity BC is set equal to 12.36 m/s with 1% turbulence intensity. The outlet-reference pressure is set equal to 72.55 kPa, while the lateral domain surfaces are defined as translational-periodic. Symmetry boundary conditions are applied to the top and bottom surfaces, and no-slip conditions are enforced to the hydrofoil walls, both on the suction and pressure sides. The configuration corresponds to a hydrofoil angle of attack of 4°. To stabilize fluid flow convergence, an initial inlet pressure of 150 kPa is set. A time step equal to 1.0E-05 s is adopted for the time advancement, ensuring a maximum Courant number condition on the order of 1E+01. Since the validation of the turbulence and cavitation model combination focuses on the streamwise sampling of the pressure coefficients on the hydrofoil suction side (see Sub-section 3.3), the authors have previously demonstrated that the spanwise domain extension has negligible influence on the static pressure field (Evangelisti et al., 2023b).

Therefore, a domain thickness of 10% of the chord length is used in the simulations, with the aim of analyzing the suction side pressure coefficients on the domain central slice, at z = 7.0E-03 m, as shown in the results presented in Fig. 9.

According to the experimental work of Shen and Dimotakis (1989), flow properties were computed at a reference temperature of 298 K, leading to a corresponding vapour pressure p_v = 3.2 kPa. Under these thermodynamic conditions ρ_l = 997.7 kg/m^3 and μ_l = 9.25E-4 Pa s represent the liquid water density and dynamic viscosity values, respectively. Considering the above-mentioned values of outlet pressure p_{out} and inlet velocity U_∞, the cavitation-regime aggressiveness is described for the hydrofoil test-case introducing the definition of the cavitation number σ_H:

$$\sigma_H = \frac{p_{out} - p_v}{\frac{1}{2}\rho_l U_\infty^2} \tag{17}$$

The mass flow rate, computed on the inlet conditions, is 97.11 kg/s and the Reynolds number based on the inflow velocity and the hydrofoil chord length, given by $Re_H = (\rho_l U_\infty c_H) / \mu_l$, is equal to 2.0E+06.

The computational domain and the simulative setup were widely tested in the precedent work of (Evangelisti et al., 2023b) where two cavitating conditions were investigated. Here, the severe cavitation condition, identified by σ_H = 0.91, was used to evaluate the ability of the model in reproducing the attached cavitation length on the hydrofoil profile. BCs values for the NACA 66 (mod) simulations are summarized in Table 1.

A first-order upwind spatial discretization method is selected for turbulent kinetic energy, specific dissipation rate, density and vapour volume fraction. Additionally, momentum is discretized with a second order upwind method. Pressure and velocity are coupled according to the SIMPLEC scheme and the spatial discretization of pressure is realized adopting the PRESTO! method. Finally, a first-order implicit method is selected for temporal discretization (ANSYS Inc., 2021c).

An intermediate unstructured grid-layer between the boundary layer region and

the far field flow zone was implemented to reduce the computational effort, resulting in a total of 2.2E+06 grid cells. The computational grid of the hydrofoil is presented in Fig. 3 (a) and (b), with Fig. 3 (a) showing the rectangular mesh global visualization and Fig. 3 (b) focusing on the hydrofoil's leading-edge and the intermediate unstructured grid-layer. The rear part of the hydrofoil profile is formed by a blunt trailing-edge, whose fluid region has been meshed through a structured boundary layer, in the same way of Fig. 3 (b). Everywhere on the NACA 66 (mod) surface, the height of the first cell of the wall was a priori calculated using a y^+=1, and its value had been continuously monitored during simulation computation. Values of y^+ never exceed 10, as shown in Fig. 4.

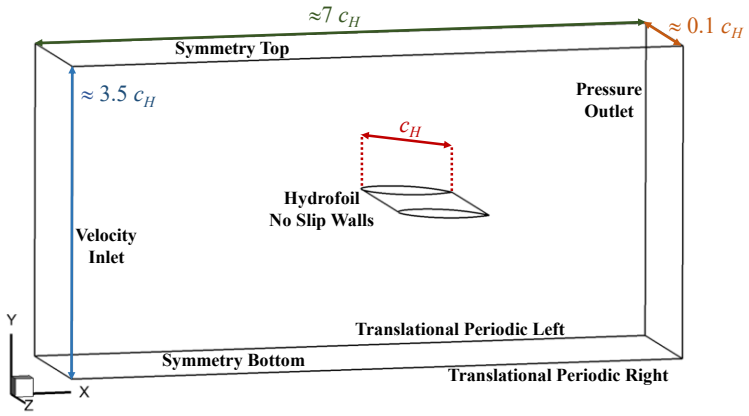

Fig. 2 NACA 66 (mod) computational domain and related BCs setting. Domain extensions are given as function of the hydrofoil chord length c_H.

Table 1 NACA 66 (mod) numerical simulations: boundary conditions (BCs) and fluid properties computed at a reference temperature of 298 K.

Boundary conditions	Numerical values
Velocity inlet, U_∞ (m/s)	12.36
Pressure inlet (initial), p_{in} (kPa)	150
Pressure outlet, p_{out} (kPa)	72.55
Vapour pressure, p_v (kPa)	3.2
Liquid water density, ρ_l (kg/m^3)	997.4
Vapour water density, ρ_v (kg/m^3)	2.3E-2
Liquid water dynamic viscosity, μ_l (Pa s)	9.25E-04
Vapour water dynamic viscosity, μ_v (Pa s)	1.07E-05
Mass flow rate, $\dot{M}$ (kg/s)	97.11
Surface tension, γ (N/m)	0.071
Hydrofoil chord length, c_H (m)	0.15
Hydrofoil angle of attack, β_H (°)	4
Hydrofoil chord-based Reynolds number, Re_H (-)	2.0E+06
Hydrofoil cavitation number, σ_H (-)	0.91

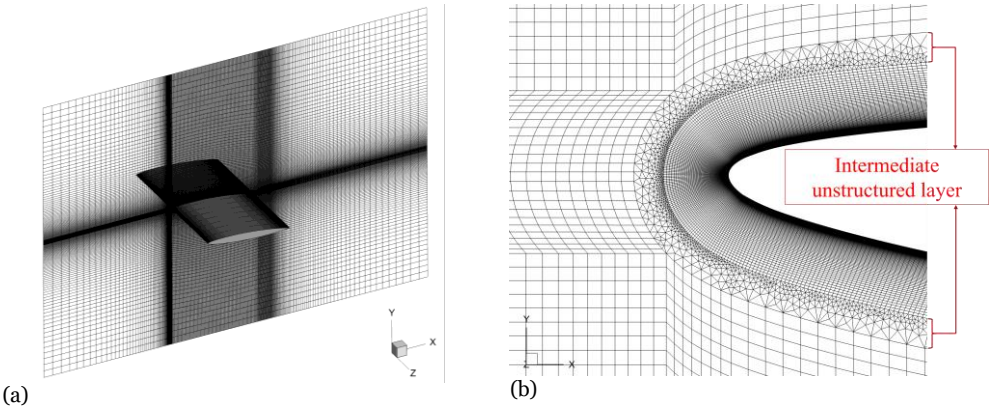

(a) (b)

Fig. 3 Test case mesh: computational grid displayed on the central slice, z = 7.0E-03 m (a) and x-y view approaching the hydrofoil leading-edge. Boundary and far field structured regions are separated by the presence of an intermediate unstructured layer (b).

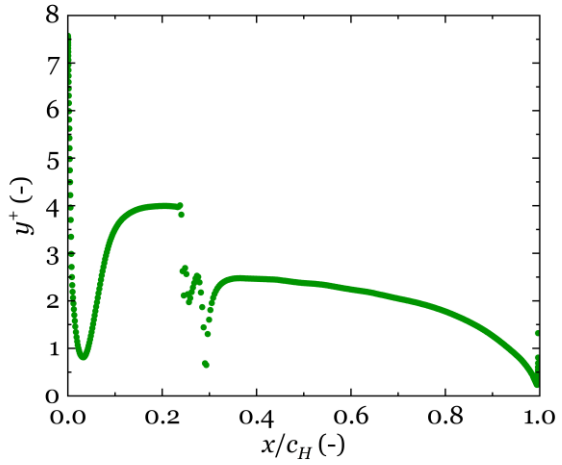

Fig. 4 y^+ values sampled on the hydrofoil suction side. CFD results are averaged in the time interval t = 0.05 s – 0.30 s and reported at the intersection between the suction side surface and the x-y central slice, z = 7.0E-03 m.

Time averaged y^+ values show a region of discontinuity for $0.25 \leq x/c_H \leq 0.30$. As further discussed in Sub-section 3.3, this is ascribed to the instability of the cavity detachment due to the static pressure recovery.

Validation of the adopted models is carried out by comparing experimental and numerical pressure coefficients on the hydrofoil suction side. The analytical pressure coefficients $C_{p,H}$ were computed according to the following formula:

$$C_{p,H}\left(x/c_H\right) = \frac{p_{out} - p\left(x/c_H\right)}{\frac{1}{2}\rho_l U_\infty^2} \tag{18}$$

In eq. (18), x/c_H represents a normalized coordinate for the hydrofoil suction side where pressure coefficients are sampled: x/c_H = 0 and x/c_H = 1 represents the profile leading and trailing-edges, respectively. Validation results will be shown in Sub-section 3.3.

3.2 Tidal turbine domain

A scaled tidal turbine domain was designed to assess the inception of cavitation under various conditions. Building on a previous study by Evangelisti et al., 2023a, the Wortmann FX63-137 blade profile was selected for the turbine geometry. Preliminary simulations, conducted as part of the domain validation process, aimed to replicate the experimental data presented by Ellis et al. (2018). For this purpose, the steady state SST k-ω turbulence model was adopted. The computational grid was defined to assess the behavior of one-third of the whole rotor extent. The turbine radius R_T is slightly higher than 0.45 m and it includes the radial lengths of the hub, the stanchion and one blade. The domain maximum extensions as function of the turbine radius are 60 R_T × 13 R_T × 22 R_T in the streamwise, radial and spanwise directions, respectively. In Fig. 5 the 120° segment domain is reported together with the applied BCs, assumed from the work of Ellis et al. (2018). The inlet velocity is constant and equal to 1 m/s. The reference outlet pressure, as well as the initial value of the inlet pressure for the simulation initialization, are chosen equal to 101.33 kPa. Fluid properties are computed at the reference temperature of 300 K. In this regard, steady simulations are carried out adopting liquid water density and dynamic viscosity of 996.5 kg/m^3 and 8.51E-04 Pa s, respectively. According to the reported inlet conditions, simulations involve a fluid mass flow rate of 3.6E+04 kg/s. All the BCs are summarized in Table 2. As previously reported in the work of Ellis et al. (2008), turbine rotation is considered by adopting a Multiple Reference Frame (MRF) model, suitable to take into account rotation in one-rotor stage machines (ANSYS Inc., 2021c). The dimensions of the MRF volume surrounding the turbine geometry (Fig. 5) were assumed according to a previous sensitivity analysis carried out by Ellis et al. (2008). The angular velocity w was varied to reproduce twelve different Tip Speed Ratio (TSR or λ) conditions, available from Ellis et al. (2008):

$$w(\lambda) = \frac{U_\infty \lambda}{R_T} \tag{19}$$

The whole set of rotating conditions as well as the turbine angle of attack β_T and the turbine Reynolds number Re_T are reported in Table 3. Tip values of the blade chord length c_T and flow total velocity v were adopted for the turbine Reynolds number computation: $Re_T = (\rho_l v c_T)/\mu_l$ where $v = \sqrt{U_\infty^2 + (wR_T)^2}$.

The domain lateral surfaces, separated by an angle of 120°, are rotational-periodic while a slip condition is applied on the top closing surface. Turbine blade, stanchion and hub are treated as walls and no-slip boundary conditions are set.

During simulations, only blade and stanchion are considered as rotating walls in the absolute reference frame. The turbine hub is modeled as a static wall, since the latter is designed to be physically integral with the support truss (except for that surface region located near the rotor and connected to the blade root via the stanchion). This reasoning was numerically verified by the authors, assuring the negligible contribution of the hub to the overall power and thrust outputs of the machine (eqs. (20, 21)).

A second-order upwind spatial discretization method is selected for momentum, turbulent kinetic energy, specific dissipation rate and density. Pressure and velocity are coupled according to the SIMPLEC scheme, while the spatial discretization of pressure is realized adopting the PRESTO! method (ANSYS Inc., 2021c).

The MSA is performed by considering four different computational grids, characterized by an increasing number of cells, as summarized in Table 4. All the computational meshes are non-structured with a polyhedric cells shape. Starting from Mesh 1, the subsequent computational grids were obtained by doubling the nodes number in the MRF region with respect to the previous mesh case.

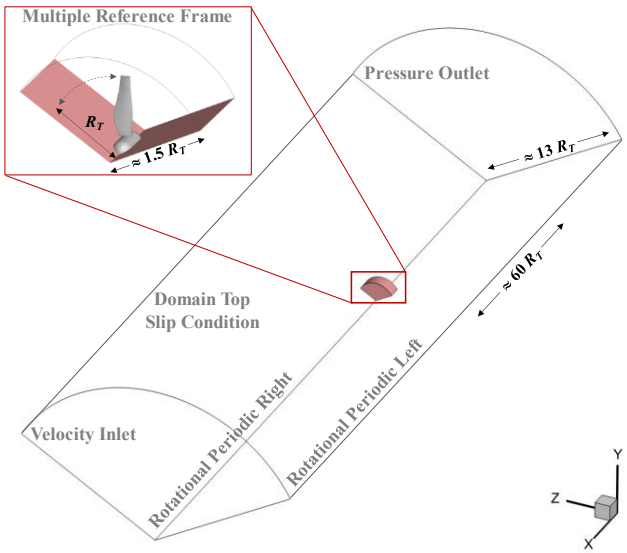

Fig. 5: 120° - scaled HATT domain and related BCs setting. domain extensions are given as function of the turbine radius R_T. in the MRF region, no slip walls are applied on the machine blade, hub and stanchion. turbine rotates clockwise, referring to the negative x-axis orientation: $\vec{w} = w(-\hat{x})$.

Table 2 Scaled HATT numerical simulations: boundary conditions (BCs) and fluid properties computed at a reference temperature of 300 K. Water vapour properties refer to the unsteady-cavitating simulations, reported in Section 4.

Boundary conditions	Numerical values
Velocity inlet, U_∞ (m/s)	1
Pressure inlet (initial), p_{in} (kPa)	101.33
Pressure outlet, p_{out} (kPa)	101.33
Vapour pressure, p_v (kPa)	3.5
Liquid water density, ρ_l (kg/m^3)	996.5
Vapour water density, ρ_v (kg/m^3)	2.5E-02
Liquid water dynamic viscosity, μ_l (Pa s)	8.51E-04
Vapour water dynamic viscosity, μ_v (Pa s)	9.76E-06
Mass flow rate, $\dot{M}$ (kg/s)	3.6E+04
Surface tension, γ (N/m)	0.071
Turbine radius, R_T (m)	0.452
Turbine tip chord length, c_T (m)	0.058

Power and thrust coefficients ($C_{Q,T}$ and $C_{F,T}$, respectively) are computed from the converged flow fields, extending the one-blade results to the whole rotor extension. As reported in eqs. (20, 21), the whole rotor calculation is taken into account by introducing a multiplicative factor equal to 3, corresponding to the number of turbine blades in the real scaled prototype:

$$C_{Q,T}(\lambda) = \frac{3\, q(\lambda)\, w(\lambda)}{\frac{1}{2}\rho\, \pi\, R_T^2\, U_\infty^3} \tag{20}$$

$$C_{F,T}(\lambda) = \frac{3\, \tau(\lambda)}{\frac{1}{2}\rho\, \pi\, R_T^2\, U_\infty^2} \tag{21}$$

Table 3 Turbine tip angle of attack β_T, total velocity v and chord-based Reynolds number Re_T computed as functions of twelve TSR experimental conditions (Ellis et al., 2008).

TSR, λ	β_T (°)	v (m/s)	Re_T (-)
1.40	27.50	1.72	1.18E+05
1.51	25.65	1.81	1.23E+05
1.78	21.32	2.05	1.40E+05
1.98	18.87	2.22	1.51E+05
2.50	13.87	2.69	1.84E+05
3.01	10.43	3.17	2.16E+05
3.47	8.14	3.61	2.46E+05
3.59	7.64	3.72	2.54E+05
4.00	6.08	4.13	2.82E+05
4.47	4.67	4.58	3.12E+05
4.94	3.51	5.04	3.44E+05
5.51	2.34	5.60	3.82E+05

Table 4 Total number of cells and peak-power maxima y^+ for each tested mesh in the HATT validation procedure

Case:	Mesh 1	Mesh 2	Mesh 3	Mesh 4
Total cells Number (-):	5.1E+06	5.7E+06	12.3E+06	33.3E+06
Max y^+ (TSR=3.59):	1.0E+02	7.8E+01	2.5E+01	2.3E+01

In eqs. (20, 21) q represents the one-blade contribution to the torque while τ is the thrust force exerted by the flow on the single turbine blade. Turbine power and thrust force are given by $Q_T(\lambda) = 3\ q(\lambda)\ w(\lambda)$ and $F_T(\lambda) = 3\ \tau(\lambda)$, respectively.

Three TSR conditions were selected for the MSA. The peak point of the power curve, corresponding to λ = 3.59, represents the rated power turbine configuration. This point, along with the preceding point (λ = 3.47) and the subsequent point (λ = 4.00), were chosen for analysis. These latter are reported further below in Fig. 10, where the experimental peak-power point is highlighted together with its measured value of power coefficient (Ellis et al., 2018).

Fig. 6 shows the sensitivity of power coefficients to different mesh sizes. The results gradually decrease from Mesh 1 to Mesh 3, with no further improvements between Mesh 3 and Mesh 4. The analysis of thrust coefficients, depicted in Fig. 7, confirms the same trend. As the grid node density increases, the thrust force stabilizes near the Mesh 3 configuration. Similarly, Mesh 4 does not provide any further numerical improvement. Consequently, Mesh 3 is selected as the computational grid for studying the behavior of the scaled geometry tidal turbine in this analysis.

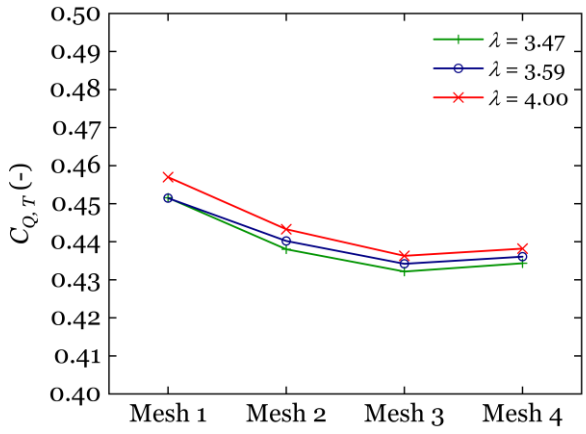

Fig. 6 MSA: Power coefficients are compared for four different meshes. Results are obtained for three TSR conditions, namely λ = 3.47, λ = 3.59 (turbine design condition) and λ = 4.00.

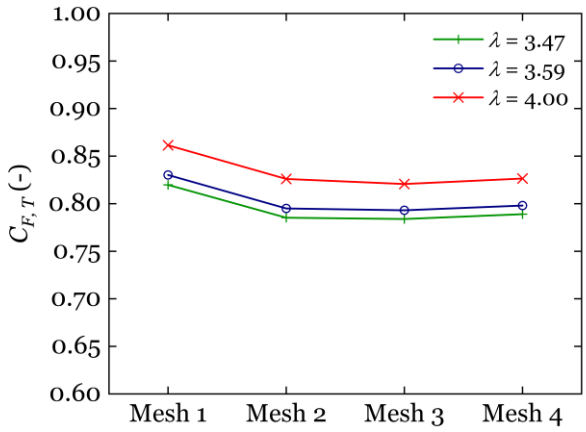

Fig. 7 MSA: Thrust coefficients are compared for four different meshes. Results are obtained for three TSR conditions, namely λ = 3.47, λ = 3.59 (turbine design condition) and λ = 4.00.

The HATT mesh topology is shown in Fig. 8. Although the displayed computational grid refers to Mesh 3, all the designed meshes share the same polyhedral unstructured characteristics. The refinement of the computational grids was achieved by uniformly modifying the number of nodes exclusively in the MRF region.

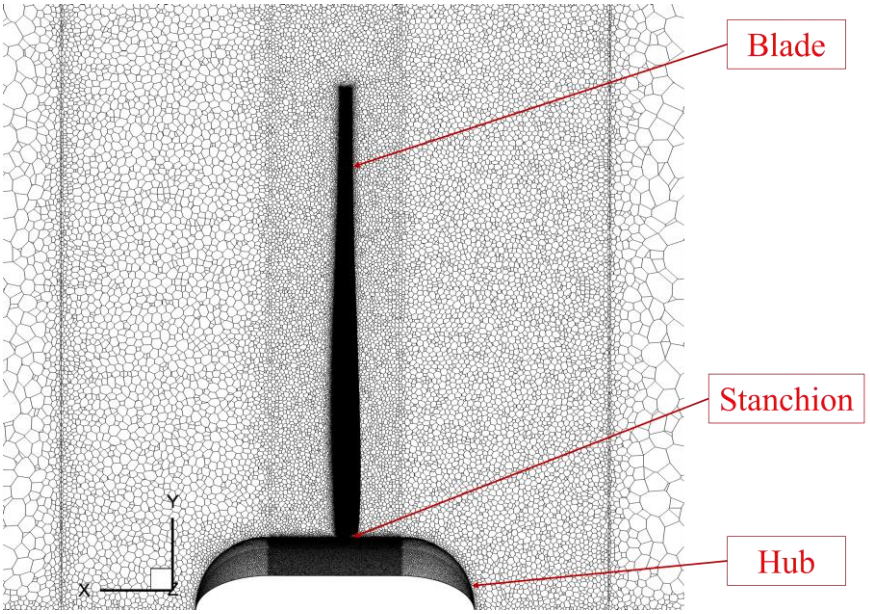

Fig. 8 Mesh 3 topology. The computational grid visualization is displayed in the MRF region around the turbine walls, on the central plane, where z = 0. The mesh is full made of polyhedric cells shape.

3.3 Models validation

As a first validation step, this Sub-section demonstrates the efficacy of the numerical approach in reproducing the cavitation formation around a hydrofoil profile. Fig. 9 presents a comparison between the experimental data from Shen and Dimotakis (1989) and the numerical results. The Singhal et al. (2003) cavitation model is applied first with the standard SST k-ω turbulence model, and then with the Reboud-corrected SST k-ω model. Numerical values of the suction side static pressure are sampled in proximity of the mid-plane, where z = 7.0E-03 m. As cavitation is a time-dependent phenomenon, influenced by turbulence fluctuations, average values were computed. Time statistics were adopted to make the evaluation of results comparable with experimental data. Statistics were collected in the time interval t = 0.05 s – 0.30 s, a time period long enough to guarantee stabilization of the average values. The modification in the eddy viscosity calculation (eq. (1)) enables a more accurate reproduction of the cavitation length, extending up to x/c_H = 0.35 in contrast to the results without the Reboud correction (Reboud et al., 1998). In fact, without this correction, the last two experimental points belonging to the cavitation length are not captured (see Fig. 9). Beyond 40% of the suction-side chord length, the recovery of the hydraulic head becomes dominant, leading to the detachment of the cavitation cloud, a phenomenon known as shedding. This instability significantly impacts the aft region of the hydrofoil, causing greater discrepancies between experimental and predicted coefficients. The largest deviation occurs at the interface between the trailing edge of the cavitation cloud and the onset of the pressure recovery zone, around x/c_H = 0.45

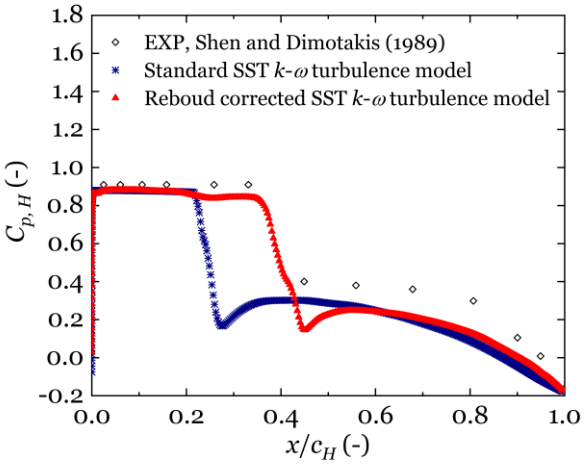

Fig. 9 Experimental (Shen and Dimotakis, 1989) and numerical pressure coefficients sampled on the hydrofoil suction side. CFD results are averaged in the time interval t = 0.05 s – 0.30 s and reported at the intersection between the suction side surface and the x-y central slice, z = 7.0E-03 m. Numerical simulations are performed by combining the Singhal et al. (2003) cavitation model with the standard and the Reboud corrected SST k-ω turbulence models.

It should be noted that, since the solver models the fluid flow as incompressible, the shedding of smaller vapor structures from the attached cavity in this case can only be attributed to the re-entrant jet mechanism (Ganesh et al., 2016). A more detailed interpretation of this phenomenon, involving compressible solvers to capture shedding caused by vapor cloud collapses, along with stricter conditions on mesh y^+ values and Courant numbers, would provide a more accurate representation of the flow characteristics. However, such an approach would come with higher computational costs, particularly when investigating the instability region in the rear portion of the hydrofoil suction side.

Given the improved alignment with the experimental data from Shen and Dimotakis (1989), the combination of the Singhal et al. (2003) cavitation model with the Reboud-corrected SST k-ω turbulence model was selected to predict the cavitating flow in the case of the HATT. In the next step, the flow field around the tidal turbine was evaluated by validating the scaled HATT geometry through a comparison of experimental power and thrust coefficients, obtained by Ellis et al. (2018), with the current simulation results (Figs. 10, 11).

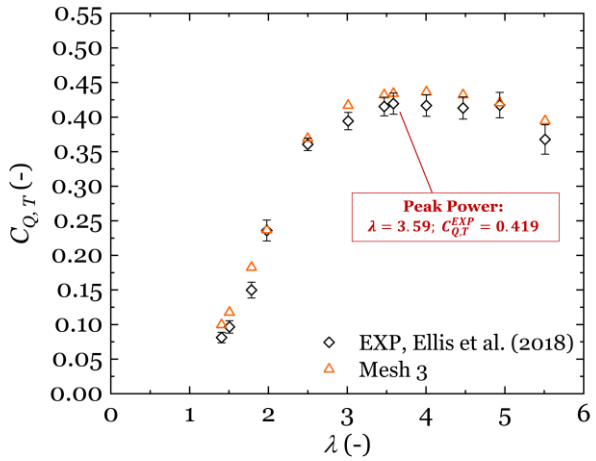

Fig. 10 Power coefficients comparison. Experimental, Ellis et al. (2018), and numerical power coefficients (Mesh 3) are compared for twelve different TSR conditions.

The power coefficients predicted in all the twelve TSR conditions exhibit a consistent physical trend in good agreement with the experimental data, as illustrated in Fig. 10. In the highest performance region, $3.47 \leq \lambda \leq 4.94$, numerical results are consistently within the experimental error band gap. A small exception is made for the last and central curve points, at $\lambda = 5.51$ and $\lambda = 3.01$, respectively, in which the predicted results are slightly higher than the experimental error band. The highest deviations are predicted in the lowest performance region points, $1.40 \leq \lambda \leq 1.78$, where the machine is approaching the stand-off condition. A quite accurate reproduction of the experimental data is instead obtained for $\lambda = 1.98; 2.50; 4.94$.

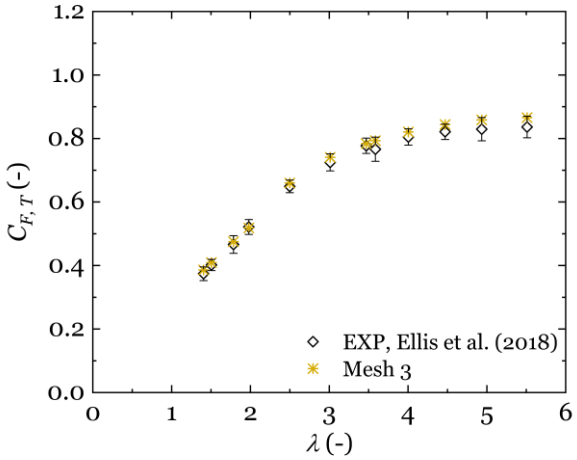

Fig. 11 Thrust coefficients comparison. Experimental, Ellis et al. (2018), and numerical thrust coefficients (Mesh 3) are compared for twelve different TSR conditions.

Furthermore, the numerical thrust coefficients are verified by comparing them with the experimental data, as illustrated in Fig. 11. In the highest TSRs region, $3.00 \leq \lambda \leq 5.51$, predicted results are always inside the experimental error band gap. Instead, in the lowest part of the curve, $1.40 \leq \lambda \leq 2.50$, computed results show a remarkable agreement with the experimental values.

In Table 5 experimental data elaborated by Ellis et al. (2018) are compared to

numerical values computed with CFD simulations using Mesh 3, for both power and thrust coefficients, in all the twelve TSR conditions. Moreover, results quality is evaluated in terms of relative errors computed as:

$$\varepsilon_{Q,T}^{EXP-CFD} = 100 \times \frac{\left| C_{Q,T}^{EXP} - C_{Q,T}^{CFD} \right|}{C_{Q,T}^{EXP}} \tag{22}$$

$$\varepsilon_{F,T}^{EXP-CFD} = 100 \times \frac{\left| C_{F,T}^{EXP} - C_{F,T}^{CFD} \right|}{C_{F,T}^{EXP}} \tag{23}$$

In eqs. (22, 23), $\varepsilon_{Q,T}^{EXP-CFD}$ and $\varepsilon_{F,T}^{EXP-CFD}$ represent the relative errors on power and thrust between experimental and predicted values, while $C_{Q,T}^{EXP}$, $C_{Q,T}^{CFD}$, $C_{F,T}^{EXP}$ and $C_{F,T}^{CFD}$ are the experimental power coefficients (Ellis et al., 2018), the numerical power coefficients (Mesh 3), the experimental thrust coefficients (Ellis et al., 2018) and the numerical thrust coefficients (Mesh 3), respectively.

Table 5 Comparison between experimental and numerical power and thrust coefficients obtained with Mesh 3. Results are provided for all the twelve TSR conditions, reporting the associated relative errors.

TSR, λ	$C_{Q,T}^{EXP}$ (–)	$C_{Q,T}^{CFD}$ (–)	$\varepsilon_{Q,T}^{EXP-CFD}$ (%)	$C_{F,T}^{EXP}$ (–)	$C_{F,T}^{CFD}$ (–)	$\varepsilon_{F,T}^{EXP-CFD}$ (%)
1.40	0.081	0.100	22.58	0.374	0.386	3.21
1.51	0.097	0.118	21.81	0.402	0.409	1.93
1.78	0.150	0.183	21.98	0.466	0.475	1.91
1.98	0.236	0.237	0.35	0.521	0.518	0.56
2.50	0.361	0.369	2.36	0.649	0.660	1.63
3.01	0.394	0.417	5.75	0.725	0.741	2.18
3.47	0.415	0.432	4.07	0.777	0.784	0.88
3.59	0.419	0.434	3.52	0.766	0.793	3.52
4.00	0.417	0.436	4.71	0.805	0.821	1.99
4.47	0.413	0.432	4.61	0.821	0.844	2.77
4.94	0.417	0.420	0.74	0.829	0.859	3.51
5.51	0.368	0.395	7.34	0.836	0.866	3.54

The results presented and discussed in this Section demonstrated that the adopted numerical approach accurately predict the cavitation phenomenon on the HATT (Section 4).

4 Cavitation prediction on the HATT

The scaled HATT geometry, previously introduced and validated in Sub-sections 3.2 and 3.3, is again used to predict cavitation occurrence around its rotor. The numerical setup remains unchanged from Sub-section 3.2, with transient and cavitating simulations employing first-order upwind spatial discretization for the vapor volume fraction and first-order implicit temporal discretization for the transient formulation (ANSYS Inc., 2021c). The simulation setup mirrors that of Sub-section 3.2, with the addition of fluid flow properties extended to the vapor phase, as outlined in Table 2. Based on the MSA carried out in Sub-section 3.2, Mesh 3 was chosen as the computational grid. Cavitation is modelled activating the Singhal et al. (2003) cavitation model in conjunction with the turbulent viscosity correction proposed by Reboud et al. (1998) and implemented through the writing of a UDF, suitable for the activated turbulence model (ANSYS Inc., 2021a).
Different conditions were assessed, verifying the cavitation occurrence for four operating regimes: cut-in (λ = 1.40), peak-power (λ = 3.59), the curve-limit angular velocity (λ = 5.51) and an off-set velocity condition, outside from the turbine designed velocities range, associated to λ = 9.03 and characterized by Re_T = 6.20E+05. A time-

dependent numerical framework is adopted to capture cavitation formation and evolution. A time step size of 1.0E-04 s was used for the first three cases, while in the highest velocity condition the time step size was decreased to 1.0E-05 s to ensure a maximum Courant number less than 10. A total flow time of 5.0E-02 s was simulated. As the rotating velocities increase, moving from λ = 1.40 to λ = 9.03, cavitation formation on the machine blade surface will be correlated with the change in the tip angles of attack β_T and the turbine cavitation number σ_T:

$$\sigma_T = \frac{p_{out} - p_v}{\frac{1}{2}\rho_l v^2} \tag{24}$$

The investigated set of cavitating conditions is summarized in Table 6.

Table 6 Tip angles of attack β_T and turbine cavitation number σ_T for the four tested TSRs conditions.

Rotating condition:	Cut-in (λ = 1.40)	Peak-power (λ = 3.59)	Curve max w (λ = 5.51)	Off-set (λ = 9.03)
β_T (°):	27.50	7.64	2.34	-1.62
σ_T (-):	66.04	14.17	6.26	2.38

When an angular velocity corresponding to λ = 1.40 is set, leading to β_T = 27.50 °, cavitation formation is mainly concentrated in proximity of the leading-edge. Maximum cavitation formation is reached for t = 2.5E-02 s. In Fig. 12 (a) it is possible to observe that the highest levels of vapour volume fraction α are concentrated along the radius extent.

The cavitating zone undergoes an enlargement starting from a height equal to half the turbine radius, Fig. 12 (b). The maximum value reached by α is close to 1.4%. No other machine regions are affected by vapour formation.

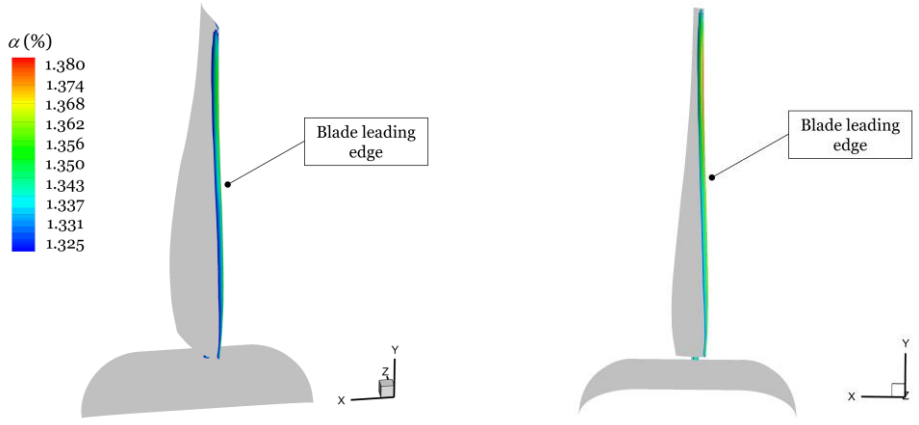

(a) (b)

Fig. 12 Contour plot of the vapour volume fraction α when λ = 1.40, t = 2.5E-02 s. Global visualization of the maximum vapour formation (a) and focus on the leading-edge attached cavity development (b) .

By increasing the angular velocity up to λ = 3.59 a sharp drop in the angle of attack value, equal to 7.64 °, is detected. In this case, a different cavitation formation is observed. The extension of the interested region becomes wider on the blade suction side, as confirmed by Fig. 13 (a). The highest values of α, whose maximum is close to 1.6%, are encountered in proximity of the blade tip, near the leading and trailing-edges, respectively, Fig. 13 (b). The peak of α is reached for the simulated instant t = 4.0E-02 s.

The third investigated case characterized by λ = 5.51 and β_T = 2.34 °, shows a similar cavitation formation compared to λ = 3.59. Higher values of α are concentrated on the blade suction side and tip regions. The maximum value of α is slightly higher than 2.8% and it is reached for t = 3.5E-02 s, Fig. 14 (a - b). Moving from a low rotating condition (λ = 1.40) to a larger TSR value (λ = 3.59) the distribution of α varies drastically.

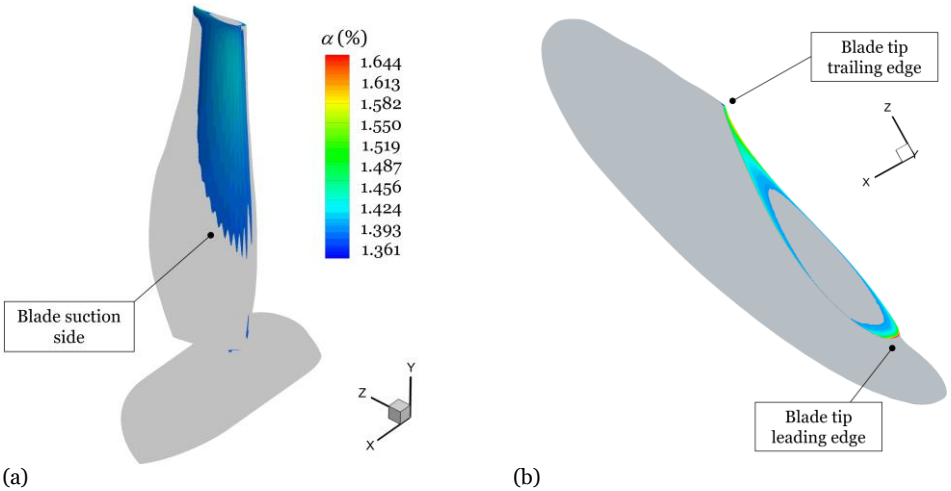

(a) (b)

Fig. 13 Contour plot of the vapour volume fraction α when λ = 3.59, t = 4.0E-02 s. Global visualization of the maximum vapour formation (a) and focus on the tip-edges attached cavity development, view of the blade top (b).

The change in the angular velocity leads to a shift of the vapour formation towards the back of the turbine suction side and the top of the blade extent. The change in the cavitation occurrence areas is related to the drop of the profile β_T values. In fact, when these latter are high enough, as in the cut-in condition, (λ = 1.40, β_T = 27.50 °) flow separation is close to the blade leading-edge where the highest values of α are detected. The increase in the angular velocity, when evaluating the peak-power (λ = 3.59, β_T = 7.64 °) and the highest rotating velocity (λ = 5.51, β_T = 2.34 °) conditions, lead to a delay in the profile-flow separation. In these latter cases a wide suction side area becomes covered by vapour, with peak values of α reached at the blade tip, where the velocities are at their maximum.

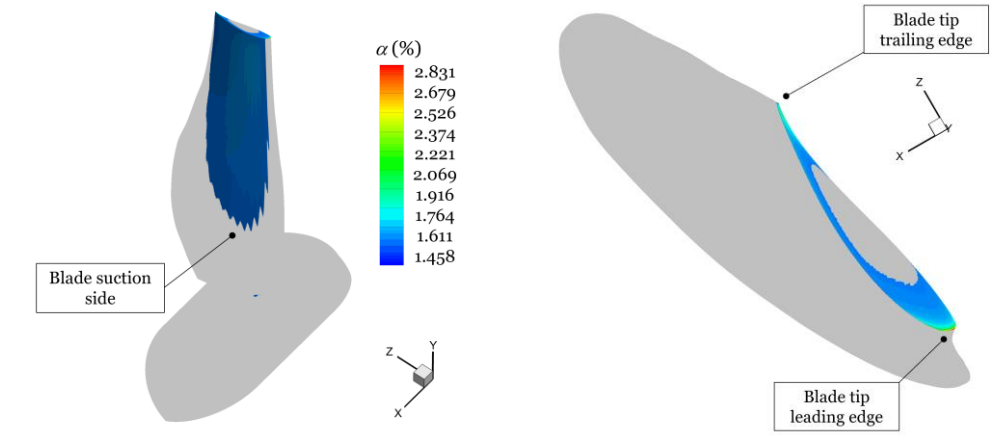

(a) (b)

Fig. 14 Contour plot of the vapour volume fraction α when λ = 5.51 and t = 2.8E-02 s. Global visualization of the maximum vapour formation (a) and focus on the tip-edges attached cavity development, view of the blade top (b).

As the angular velocity is increased till the off-set condition, λ = 9.03, β_T = -1.62 °, the vapour formation changes drastically. In this last case, higher values of α are globally detected, as shown in Fig. 15 (a). The maximum of α is close to 93% when t = 3.0E-02 s. The negative angle of attack leads to a more specific location on the tip of the turbine blade, Fig. 15 (b).

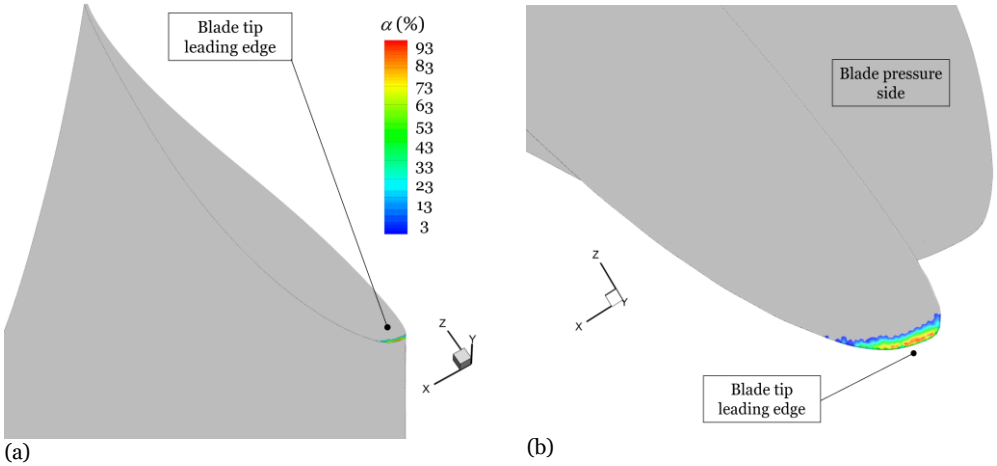

Fig. 15 Contour plot of the vapour volume fraction α when λ = 9.03 and t = 3.0E-02 s. Visualization of the maximum vapour formation from the top leading-edge view (a) and zoom on the tip leading-edge attached cavity development, view of the blade top (b).

Different cavitation occurrence zones can physically lead to different cavitation-erosion potential damaged areas. As in the first investigated case the cavitation-formation region develops in proximity of the turbine leading-edge, one may expect an ensuing erosive damage which is more likely distributed along the turbine radial extent. On the other side, when the peak-power and the highest TSR conditions are set, the most exposed region to cavitation-formation is distributed on a larger surface, with the blade tip region becoming more critical. The wider cavitation onset can trigger a different erosive pattern, which is in this case a consequence of the shift in the vapour formation, towards the blade suction side and tip.

The final off-set regime highlights a different cavitation displacement, localized on the tip leading-edge and described by higher values of α. Although the predicted cavitation behavior results in a reduced affected area, its aggressiveness is noticeably increased.

5 Conclusions

In this paper, the cavitation inception in a scaled geometry tidal turbine is evaluated using numerical simulations. The validation of turbulence and cavitation models is conducted by comparing experimental and numerical pressure coefficients for a NACA 66 (mod) hydrofoil. The modified model, with the introduction of the eddy viscosity correction, allows for a complete reproduction of the cavitation length. A MSA is performed on the scaled tidal turbine model, by comparing numerical results obtained using four different computational grids with experimental data. Among the tested meshes, Mesh 3 represents the best compromise computational grid, showing a satisfactory agreement in reproducing the experimental power and thrust coefficients trend.

Cavitation is then assessed for the HATT by combining the validated models in a

single one. In general, for the four investigated TSR conditions, cavitation shows different behaviors. At the lowest rotating velocity, λ = 1.40 when the tip β_T = 27.50 °, the highest values of α are concentrated along the blade leading-edge, while at rated power, λ = 3.59 when the tip β_T = 7.64 °, an extended region affected by increasing α is recognized in the upper part of the blade suction side. The curve highest rotating velocity condition (λ = 5.51, β_T = 2.34 °) substantially denotes a similar behavior as that described for λ = 3.59. When the angular velocity is increased up to λ = 9.03 and β_T = -1.62 °, the cavitation region becomes more localized on the blade tip leading-edge. In this off-set condition the highest values of α are registered (93%). This behavior can be explained by relating the cavitation occurrence areas with the computed β_T of the blade profile. Starting from the initial working condition in which β_T = 27.50 ° for λ = 1.40, the increase in the rotating velocity leads to quite comparable values of the tip angle of attack: β_T = 7.64 ° for λ = 3.59 and β_T = 2.34 ° for λ = 5.51. In these two intermediate regimes the higher values of α appear in a delayed region of the blade profile suction side, in proximity of the blade tip leading and trailing-edges. The reduction of β_T affects the low pression areas position, which shifts toward the rear as the rotating velocity increases. When the tip angle of attack becomes negative, β_T = -1.62 ° for λ = 9.03, a different interested area is predicted, totally localized on the tip leading-edge. The severity of the off-set cavitating condition is testified by the highest values of α which may potentially lead to severe erosion phenomena over time.

Funding

The authors of this paper declare that the work presented in this manuscript has been developed and carried out with no funding.

References

Alam, P., Robert, C., & Ó Brádaigh, C. M. (2018). Tidal turbine blade composites - A review on the effects of hygrothermal aging on the properties of CFRP. *Composites Part B: Engineering*, *149*, 248–259. https://doi.org/https://doi.org/10.1016/j.compositesb.2018.05.003

ANSYS Inc. (2021a). *ANSYS Fluent Customization Manual 21.2*.

ANSYS Inc. (2021b). *ANSYS Fluent Theory Guide 21.2* .

ANSYS Inc. (2021c). *ANSYS Fluent User's Guide 21.2*.

Berntsen, G., Kjeldsen, M., & Arndt, R. (2001). *Numerical Modeling of Sheet and Tip Vortex Cavitation with Fluent 5*.

Bilus, I., Morgut, M., & Nobile, E. (2013). Simulation of sheet and cloud cavitation with homogenous transport models. *International Journal of Simulation Modelling*, *12*(2), 94–106. https://doi.org/10.2507/IJSIMM12(2)3.229

Capone, A., DiFelice, F., Salvatore, F., Maddukkari, H., Kaufmann, N., & Starzmann, R. (2023). Impact of cavitation and inflow perturbation on the performance of a horizontal-axis tidal turbine. *Journal of Ocean Engineering and Marine Energy*, *9*(4), 731–743. https://doi.org/10.1007/s40722-023-00296-9

Churkin, S. A., Pervunin, K. S., Kravtsova, A. Yu., Markovich, D. M., & Hanjalić, K. (2016). Cavitation on NACA0015 hydrofoils with different wall roughness: high-speed visualization of the surface texture effects. *Journal of Visualization*, *19*(4), 587–590. https://doi.org/10.1007/s12650-016-0355-9

Ducoin, A., Huang, B., & Young, Y. L. (2012). Numerical modeling of unsteady cavitating flows around a stationary hydrofoil. *International Journal of Rotating Machinery*, *2012*. https://doi.org/10.1155/2012/215678

Dular, M., Stoffel, B., & Širok, B. (2006). Development of a cavitation erosion model.

Wear, *261*(5–6), 642–655. https://doi.org/10.1016/j.wear.2006.01.020
Ellis, R., 'Allmark, M., 'O'Doherty, T., 'Mason-Jones, A., 'Ordonez-Sanchez, S., 'Johannesen, K., & 'Johnstone, C. (2018). *Design Process for a Scale Horizontal Axis Tidal Turbine Blade*. 1–8.
Evangelisti, A., Agati, G., Borello, D., Mazzotta, L., & Venturini, P. (2023). Cavitation assessment on a model scale tidal turbine. *Proceeding of 10th International Symposium on Turbulence, Heat and Mass Transfer, THMT-23, Rome, Italy, 11-15 September 2023*, 4. https://doi.org/10.1615/ICHMT.THMT-23.540
Evangelisti, A., Agati, G., Haghighifard, H., Rispoli, F., Venturini, P., & Borello, D. (2023). *Influence of turbulence models in the prediction of cavitation occurrence*. https://doi.org/10.29008/ETC2023-179
Folden, T. S., & Aschmoneit, F. J. (2023). A classification and review of cavitation models with an emphasis on physical aspects of cavitation. *Physics of Fluids*, *35*(8). https://doi.org/10.1063/5.0157926
Ganesh, H., Mäkiharju, S. A., & Ceccio, S. L. (2016). Bubbly shock propagation as a mechanism for sheet-to-cloud transition of partial cavities. *Journal of Fluid Mechanics*, *802*, 37–78. https://doi.org/10.1017/jfm.2016.425
Ghahramani, E., Ström, H., & Bensow, R. E. (2021). Numerical simulation and analysis of multi-scale cavitating flows. *Journal of Fluid Mechanics*, *922*. https://doi.org/10.1017/jfm.2021.424
Gohil, P. P., & Saini, R. P. (2014). Coalesced effect of cavitation and silt erosion in hydro turbines - A review. *Renewable and Sustainable Energy Reviews*, *33*, 280–289. https://doi.org/10.1016/j.rser.2014.01.075
Hong, S., Wu, Y., Wu, J., Zhang, Y., Zheng, Y., Li, J., & Lin, J. (2021). Microstructure and cavitation erosion behavior of HVOF sprayed ceramic-metal composite coatings for application in hydro-turbines. *Renewable Energy*, *164*, 1089–1099. https://doi.org/10.1016/j.renene.2020.08.099
Kravtsova, A. Yu., Markovich, D. M., Pervunin, K. S., Timoshevskiy, M. V., & Hanjalić, K. (2014). High-speed visualization and PIV measurements of cavitating flows around a semi-circular leading-edge flat plate and NACA0015 hydrofoil. *International Journal of Multiphase Flow*, *60*, 119–134. https://doi.org/10.1016/j.ijmultiphaseflow.2013.12.004
Kunz, R. F., Boger, D. A., Stinebring, D. R., Chyczewski, T. S., Lindau, J. W., Gibeling, H. J., Venkateswaran, S., & Govindan, T. R. (2000). A preconditioned Navier–Stokes method for two-phase flows with application to cavitation prediction. *Computers & Fluids*, *29*(8), 849–875. https://doi.org/10.1016/S0045-7930(99)00039-0
Lee, I., Park, S., Seok, W., & Rhee, S. H. (2021). A Study on the Cavitation Model for the Cavitating Flow Analysis around the Marine Propeller. *Mathematical Problems in Engineering*, *2021*. https://doi.org/10.1155/2021/2423784
Menter, F. (1993, July 6). Zonal Two Equation k-w Turbulence Models For Aerodynamic Flows. *23rd Fluid Dynamics, Plasmadynamics, and Lasers Conference*. https://doi.org/10.2514/6.1993-2906
Merkle, C. L. '. (1998). Computational modelling of the dynamics of sheet cavitation. *Proceedings of the 3rd International Symposium on Cavitation, Grenoble*.
Morgut, M., Nobile, E., & Biluš, I. (2011). Comparison of mass transfer models for the numerical prediction of sheet cavitation around a hydrofoil. *International Journal of Multiphase Flow*, *37*(6), 620–626. https://doi.org/10.1016/j.ijmultiphaseflow.2011.03.005
Padhy, M. K., & Saini, R. P. (2008). A review on silt erosion in hydro turbines. *Renewable and Sustainable Energy Reviews*, *12*(7), 1974–1987.

https://doi.org/10.1016/j.rser.2007.01.025
Reboud, J.-L., 'Stutz, B., & 'Coutier, O. (1998). Two-phase flow structure of cavitation: experiment and modelling of unsteady effects. *Third International Symposium on Cavitation*, 1–7.
Saito, Y., Takami, R., Nakamori, I., & Ikohagi, T. (2007). Numerical analysis of unsteady behavior of cloud cavitation around a NACA0015 foil. *Computational Mechanics*, *40*(1), 85–96. https://doi.org/10.1007/s00466-006-0086-1
Savio, A., Cianferra, M., & Armenio, V. (2021). Analysis of performance of cavitation models with analytically calculated coefficients. *Energies*, *14*(19). https://doi.org/10.3390/en14196425
Schnerr, G. H., & Sauer, J. (2001, May 5). Physical and Numerical Modeling of Unsteady Cavitation Dynamics. *ICMF-2001, 4th International Conference on Multiphase Flow*.
Senocak, I., & Shyy, W. (2002). Evaluation of cavitation models for Navier-Stokes computations. *American Society of Mechanical Engineers, Fluids Engineering Division (Publication) FED*, *257*(1 A), 395–401. https://doi.org/10.1115/FEDSM2002-31011
Shen, Y. T., & Dimotakis, P. E. (1989). The influence of Surface Cavitation on Hydrodynamic Forces. *Day 1 Tue, August 08, 1989*. https://api.semanticscholar.org/CorpusID:253353565
Shi, W., Atlar, M., Rosli, R., Aktas, B., & Norman, R. (2016). Cavitation observations and noise measurements of horizontal axis tidal turbines with biomimetic blade leading-edge designs. *Ocean Engineering*, *121*, 143–155. https://doi.org/https://doi.org/10.1016/j.oceaneng.2016.05.030
Singhal, A. K., Athavale, M. M., Li, H., & Jiang, Y. (2003). Mathematical basis and validation of the full cavitation model. *Proceedings of the ASME Fluids Engineering Division Summer Meeting*, *1*, 379–406.
Song, S., Demirel, Y. K., Atlar, M., & Shi, W. (2020). Prediction of the fouling penalty on the tidal turbine performance and development of its mitigation measures. *Applied Energy*, *276*, 115498. https://doi.org/https://doi.org/10.1016/j.apenergy.2020.115498
Sun, Z., Li, D., Mao, Y., Feng, L., Zhang, Y., & Liu, C. (2022). Anti-cavitation optimal design and experimental research on tidal turbines based on improved inverse BEM. *Energy*, *239*, 122263. https://doi.org/10.1016/j.energy.2021.122263
Timoshevskiy, M. V., Churkin, S. A., Kravtsova, A. Yu., Pervunin, K. S., Markovich, D. M., & Hanjalić, K. (2016). Cavitating flow around a scaled-down model of guide vanes of a high-pressure turbine. *International Journal of Multiphase Flow*, *78*, 75–87. https://doi.org/10.1016/j.ijmultiphaseflow.2015.09.014
Timoshevskiy, M. V., Zapryagaev, I. I., Pervunin, K. S., Maltsev, L. I., Markovich, D. M., & Hanjalić, K. (2018). Manipulating cavitation by a wall jet: Experiments on a 2D hydrofoil. *International Journal of Multiphase Flow*, *99*, 312–328. https://doi.org/10.1016/j.ijmultiphaseflow.2017.11.002
Young, F. R. (1999). *Cavitation*. Imperial Collage Press.
Zwart J. P., Gerber G. A ., & Belamri T. (2004). A Two-Phase Flow Model for Predicting Cavitation Dynamics. *ICMF 2004 International Conference on Multiphase Flow*.